Wave-front reconstruction and analysis of far-field high-order harmonics from relativistic plasma surfaces

Y. Zhang[1,2] L. Li,[3,*] L.F. Gan,[4] S.P. Zhu,[5] X.T. He,[1,5] Ph. Zeitoun,[2] and B. Qiao[1,†]

[1] *Center for Applied Physics and Technology, HEDPS, and SKLNPT, School of Physics, Peking University, Beijing 100871, China*

[2] *Laboratoire d'Optique Appliquée, ENSTA Paris-École Polytechnique IP Paris - CNRS, UMR 7639, Palaiseau, France*

[3] *Shenzhen Key Laboratory of Ultra-Intense Laser and Advanced Materials Technology, Center for Intense Laser Application Technology, Shenzhen Technology University, Shenzhen 518118, China*

[4] *School of Microelectronics and Physics, Hunan University of Technology and Business, Changsha 410205, China*

[5] *Institute of Applied Physics and Computational Mathematics, Beijing 100094, China*

With a numerical reconstruction algorithm proposed, the complete far-field wave-fronts of harmonics, which are emitted from relativistic plasma surfaces, have been retrieved from their complex spatial-temporal distributions. Combining theoretical analysis and three-dimensional simulations, the impact of the plasma density gradient, driving pulse quality, and polarization have been comprehensively investigated. Abundant information on the generation mechanism, optical properties, and aberration evolution of the generated harmonics, as well as the relativistic plasma surface structure are decoded from the reconstructed wave-front. Furthermore, proper defocusing incident lasers are proposed to achieve aberration-free attosecond sources at the extreme ultraviolet region with Gaussian-like intensity distribution. Providing powerful numerical tools and practical advice, current work is essential for analyzing wave-fronts, studying relativistic plasma properties and utilizing attosecond pulses in ultrafast metrology and control.

I. INTRODUCTION

Bright attosecond radiation sources with high spatial quality are essential for the ultrafast metrology and control in attosecond (1 as = 10^{-18} s) time scale [1], greatly facilitating applications in atomic [2], molecular [3], condensed matter [4], high-energy-density [5], and plasma physics [6]. With the benefit of high conversion efficiency and no limitation on the driving field [7–9], the relativistic high-order harmonic generation (RHHG) [10] from overdense plasma surfaces has become a promising table-top approach to obtain bright attosecond pulses at extreme ultraviolet (XUV) regime.

In RHHG, the plasma surfaces act like relativistic reflecting mirrors [11], which are formed and driven by incident lasers. Dynamics and properties of these plasma mirrors not only determine the cutoff frequency of harmonics [7], but also affect the near- [12–15] and far-field [16–18] properties of attosecond pulses. Among these properties, far-field wave-fronts of the RHHG harmonics depend on characteristics of driving pulses and plasma surfaces, carrying abundant information of the laser-plasma interactions. Moreover, for practical attosecond pump-probe experiments performed far from interaction areas, the wave-front quality plays a significant role on beam transmission [19], focusing [20], as well as imaging [21].

However, the wave-front study of such brilliant RHHG harmonics has not been reported either theoretically or experimentally, yet. Ptychography [22] has been used to measure the spatial properties of RHHG and plasma mirrors [13], but such *in situ* multishot characterization has to distort the initial plasma mirror and obtains only properties on one axis so far. Fortunately, the widely used Hartmann wave-front sensor [23] is suitable for the metrology of full wave-fronts. Reconstructing wave-fronts from local propagation directions of beams, Hartmann sensing technique is adequate to work with broadband sources under single exposure [24,25] and has been successfully used for the XUV microscopy [26], proving great potential in the far-field wave-front characterization and study of RHHG sources with large divergences [27]. In addition to experimental techniques, there is still a lack of a proper algorithm to directly decode the wave-front from

*lilu@sztu.edu.cn
†bqiao@pku.edu.cn

complex electromagnetic fields, which are obtained from the numerical study of RHHG sources. Such a study plays an irreplaceable role in understanding and optimizing the features of relativistic plasmas and RHHG light sources.

In this paper, we propose an efficient numerical algorithm to reconstruct the wave-fronts from spatial-temporal distributions of electromagnetic fields by borrowing principles of the Hartmann sensors and utilizing them in the frequency domain. Combining with three-dimensional (3D) simulations, we have reconstructed the complete far-field wave-fronts of harmonics emitted from RHHG and the impact of the gradient of plasma density distribution and quality of incident pulses are studied. Consistent with our theoretical analysis, abundant information on laser-plasma interactions contained in wave-fronts has been decoded, such as the RHHG mechanism, structures of plasma surfaces as well as polarization and spatial properties of the driving lasers. For far-field harmonics, the physical understanding and evolution of different aberrations of the reflected harmonics have been discussed. What is more, the proper defocusing configurations have been proposed to improve the rms errors of order-dependent aberration distributions, which are introduced by plasma surfaces, to subnanometer levels with Gaussian-like intensity distributions generated. Closely related to simulations and experiments, the present study provides effective suggestions on implementing the RHHG wave-front measurement, analysis, and study of relativistic plasma properties.

II. ALGORITHM AND THEORY ANALYSIS

The scheme of the wave-front reconstruction algorithm is illustrated in Fig. 1, where the monochromatic beam propagates along the x axis (gray fine dotted) with a fixed astigmatism aberration and Gaussian time envelope (black dashed). To reconstruct its wave-front $\Delta\Phi$ (colorful curved surface), the electric field $E(y, z, t)$ on the yz plane (green plane) is divided into different parts by moveable spatial windows (yellow square). Here, the distributions of $E(y, z, t)$ on t-y ($z = 0$) and t-z ($y = 0$) planes are illustrated on t-y ($z = z_{\min}$) and t-z ($y = y_{\min}$) planes, respectively. Then, the local propagation directions of the beam (purple arrows, θ_y and θ_z) are calculated through the first-order centroid method performed on spectral spaces. Finally, similar to Hartmann sensors, which obtain θ_y and θ_z from diffraction patterns [23], the $\Delta\Phi$ is reconstructed from its gradient information contained in θ_y and θ_z. We note that $\Delta\Phi$ is defined based on reference wave-fronts as illustrated in the inset of Fig. 1, where $\Delta\Phi > 0$ (red) if the real wave-front (solid line) is ahead of the reference one (black dashed) along the propagation direction (black arrow) otherwise $\Delta\Phi < 0$ (blue). Appendix A explains the algorithm in details with benchmark carried out.

The model of RHHG is shown in Fig. 2(a), where coordinate systems for incident lasers $Ox_iy_iz_i$, reflected
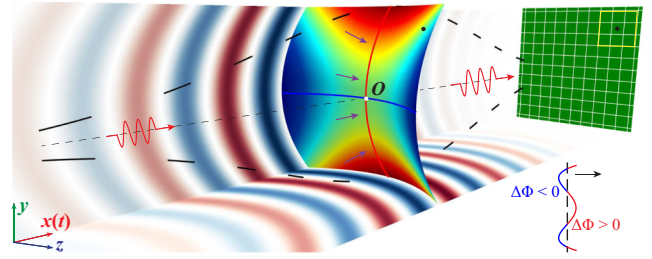

FIG. 1.   3D schematic for the wave-front reconstruction of a distorted monochromatic beam with Gaussian time envelope (black dashed), which propagates along the x axis (gray fine dotted). The way of defining the wave-front $\Delta\Phi$ (colorful curved surface) is illustrated in the inset, where the black dashed line and arrow represent the reference wave-front and the propagation direction, respectively. Local propagation directions (purple arrows) of the beam are calculated from local electromagnetic fields selected by the yellow spatial window, which moves on the y-z plane (green screen). Electric field distributions on t-y ($z = 0$) and t-z ($y = 0$) planes are shown on planes, which are parallel to them, respectively.

harmonics $Oxyz$, and targets $Ox_ty_tz_t$ have the same origin O (white dot) and z axis. Here, O is defined as the point where the incident optic axis (orange dashed) intersects with the interface (white dot-dashed) between exponential preplasma (gray block, electron density $n_e = n_0 \exp(x_t/L)$) and the main target (black block, $n_e = n_0$). In the model, a linearly polarized Gaussian driving laser (orange solid) propagates along the x_i axis (orange dashed), irradiating on an overdense plasma target obliquely with incident angle α. The focus of the incident laser is set at $(x_{i0}, 0, 0)$ and $x_{i0} = 0$ in Fig. 2(a). Then, reflected harmonics (blue solid) are generated from and refocused by the optically curved plasma mirror [7,11], resulting in the movement of harmonics foci (blue dot) from O to $(\Delta x, \Delta y, \Delta z)$ in $Oxyz$. The x axis is along the specular reflection direction of the incident laser and the x_t axis is perpendicular to the target surface. After propagating a distance x_{far}, far-field wave-fronts of harmonics (purple dashed) are reconstructed and compared with the reference spherical wave-front (red dashed), whose center and radius are O and $R_{\mathrm{ref}} = x_{\mathrm{far}}$, respectively.

Due to high harmonic generation efficiency, p-polarized (y_i-polarized) incident lasers are widely used in RHHG. As the polarization plane coincides with the $z = 0$ plane, it is easy to get $\Delta\Phi(y, z) = \Delta\Phi(y, -z)$ owing to the symmetric setting. Therefore, $\Delta\Phi$ can be expanded in power series as $\Delta\Phi = \Phi_0 + p_1 y + p_2(z^2 + y^2) + p_3(z^2 - y^2) + \Delta\Phi^{\mathrm{high}}$. According to the aberration theory [28], linear terms y and z are introduced by the transverse movement ($\Delta y, \Delta z$) of harmonics foci and the coefficients are $\Delta y/x_{\mathrm{far}}$ and $\Delta z/x_{\mathrm{far}}$, respectively. Clearly, for p-polarized incident lasers, $\Delta z = 0$. Introduced by the focusing effect of optically curved plasma mirrors [11], the quadratic term
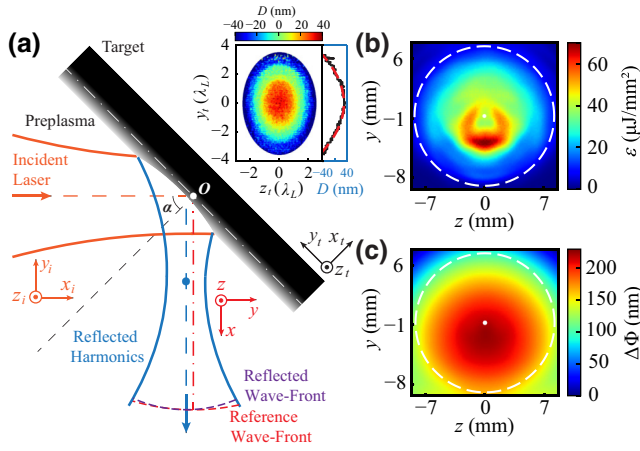
FIG. 2. (a) Schematic of the far-field wave-front (purple dashed) reconstruction for reflected harmonics (blue solid) from RHHG. Propagating along the x_i axis, the incident laser (orange solid) irradiates on an overdense plasma target (black block) with angle α, where exponential preplasma (gray block) exists. The reference spherical wave is represented by the red dashed line. Besides, the optically curved plasma mirror is indicated by the longitudinal reflection position D (relative values) of electric fields shown in the inset, whose profile on the plane $z_t = 0$ is illustrated by the black solid line and fitted by the parabolic red dashed line. (b) Far-field energy density ε distribution and (c) reconstructed far-field wave-front of the tenth harmonic ($x_{\text{far}} = 10^5 \lambda_L$), where white dot and dashed lines represent the centroid and aperture, respectively. Here, simulation parameters $L = 0.1\lambda_L$, $x_{i0} = 0$ and $\alpha = 45°$ are used.

$z^2 + y^2$ (defocusing) is associated with the longitudinal movement Δx of harmonic foci, whose coefficient $p_2 = -\Delta x / x_{\text{far}}^2$ [28]. Besides, another quadratic term $z^2 - y^2$ (astigmatism) is associated with different curvature radii of reflected harmonics on the sagittal ($y = 0$) and tangential ($z = 0$) planes. Considering the discussion above, the theoretical wave-front of harmonics from p-polarized incident lasers can be expressed as

$$\Delta\Phi \approx \Phi_0 + \frac{\Delta y}{x_{\text{far}}} y - \frac{\Delta x}{2x_{\text{far}}^2}(z^2 + y^2) + \frac{b_A}{2x_{\text{far}}^2}(z^2 - y^2). \tag{1}$$

Further, according to the derivation in Appendix B, when an aberration-free ultraintense incident Gaussian beam is used and the far-field assumption is met, we have

$$\Delta x = \frac{-R_r}{1 + \left[R_r x_R / n\beta_n^2(x_R^2 + x_{i0}^2)\right]^2}, \quad b_A = 0, \tag{2}$$

$$R_r = \frac{-\left(x_R^2 + x_{i0}^2\right)}{x_{i0} + 4\pi L x_R \cos\alpha/\lambda_L}, \tag{3}$$

where $x_R \equiv \pi w_L^2/\lambda_L$, λ_L, and w_L represent the Rayleigh length, wavelength, and beam waist at the focus of the incident laser, respectively. Here, $\beta_n \equiv w_{sn}/w_s$ is the radius ratio of the nth harmonic to the incident laser on the plasma mirror, where R_r represents the curvature radius of reflected harmonics at the same place. Furthermore, when a defocusing incident laser is used, which satisfies $x_{i0} = -4\pi L x_R \cos\alpha/\lambda_L$ [18], the focusing effect of plasma mirrors is offset and we have $\Delta x = 0$.

Besides, the coma, spherical aberration and other high-order aberrations are also expected in the $\Delta\Phi^{\text{high}}$, which are generated due to the oblique incidence [29,30], non-ideal surfaces of plasma mirrors and instability of laser-plasma interactions. Such aberrations indicate the complex dynamics of RHHG and plasma mirrors.

To verify the theoretical predictions and evaluate influence of high-order aberrations, well-known Zernike polynomials $Z_j(y, z, \rho)$ [31] are used to analyze reconstructed wave-fronts across a circular aperture C whose radius is represented by ρ. Due to the orthogonality of Z_j among C, the $\Delta\Phi$ can be expanded as $\Delta\Phi = \sum_j c_j Z_j(y, z, \rho)$ and its rms error σ (variance σ^2) can be expressed as $\sigma = \sqrt{\sum_{j=1} c_j^2}$. Comparing Eq. (1) with the definitions of $Z_j(y, z, \rho)$ provided in Appendix C, we obtain

$$\Delta z = 2c_1 x_{\text{far}}/\rho, \tag{4}$$

$$\Delta y = 2c_2 x_{\text{far}}/\rho, \tag{5}$$

$$\Delta x = -4\sqrt{3}c_3 x_{\text{far}}^2/\rho^2, \tag{6}$$

$$b_A = 2\sqrt{6}c_5 x_{\text{far}}^2/\rho^2. \tag{7}$$

Considering the physical meaning of Z_j [32], to evaluate the proportion of common aberrations presenting in optical systems, we define the σ_A, σ_C, and σ_S that are associated with astigmatism, coma and spherical aberrations, respectively, as

$$\sigma_A \equiv \sqrt{c_4^2 + c_5^2 + c_{11}^2 + c_{12}^2 + c_{22}^2 + c_{23}^2}, \tag{8}$$

$$\sigma_C \equiv \sqrt{c_6^2 + c_7^2 + c_8^2 + c_9^2 + c_{15}^2 + c_{16}^2}, \tag{9}$$

$$\sigma_S \equiv \sqrt{c_{10}^2 + c_{21}^2}. \tag{10}$$

III. SIMULATION RESULTS

To verify our reconstruction method and theoretical predictions, 3D numerical simulations are carried out by the particle-in-cell (PIC) code EPOCH [33] and the self-developed far-field electromagnetic field calculation module [17]. The time-domain near-to-far-field transformation [34] is utilized in such a module, which is based on the Kirchhoff integration. The setting of PIC simulations is explained in Sec. II and illustrated in Fig. 2(a). Without

special statements, incident lasers with Gaussian spatial and temporal envelopes are used, where the temporal full-width-half-maximum $\tau = 8$ fs, focal waist $w_L = 2$ μm, incident angle $\alpha = \pi/4$, wavelength $\lambda_L = 800$ nm, peak intensity $I_L = 1.92 \times 10^{21}$ W/cm^2 (the normalized amplitude $a_L \approx 30$), and the foci position $x_{i0} = 0$. Besides, the electron density of target bulk $n_0 = 100 n_c$ whose thickness $d = 0.5\lambda_L$, and the scale length of exponential preplasma $L = 0.1\lambda_L$. Here, $n_c \equiv m_e \omega_L^2 / 4\pi e^2$ represents the critical electron density of plasma, where ω_L is the angular frequency of incident lasers and m_e as well as e represent the mass and absolute charge of electrons, respectively. The size of the simulation box $x_i \times y_i \times z_i$ is $13\lambda_L \times 14\lambda_L \times 14\lambda_L$ ($1300 \times 1400 \times 1400$ cells) with four and two macroparticles per cell for electrons and carbon ions, respectively. Here, as the influence of the movement of ions is negligible according to theoretical analysis and numerical simulations performed in Appendix D, fixed ions are chosen to save the computational resources. As for the far-field calculation, the results are obtained on the plane $x = x_{\mathrm{far}} = 10^5 \lambda_L$.

As shown in the inset of Fig. 2(a), the optical pressure of the incident laser forms a curved plasma mirror. Here, the depth D is the relative position of the reflection point of electric fields along the x_t axis. Fitted by quadratic functions, the focal length of the plasma mirror on the tangential ($z_t = 0$) and sagittal ($y_t = 0$) planes are about 24.6 and 12.5 μm, respectively. Such simulation results well meet predictions of Eqs. (B5)–(B6) where $f_p^t \approx 25$ μm and $f_p^s \approx 12.5$ μm. Here, the real (black solid) and fitted (red dashed) values of D on the plane $z_t = 0$ are shown on the right side of the inset.

Considering the tenth reflected harmonic, which is obtained through a numerical bandpass filter, its far-field distribution of energy density ε is shown in Fig. 2(b). Due to the strong spatiotemporal coupling [19,20], deflection of the reflected harmonics [35] as well as high-order Hermite-Gaussian modes' generation introduced by the focusing effects and dynamics of nonideal plasma mirrors [36], it is far different from the Gaussian distribution. The center (y_c, z_c) (white dot) of circular aperture (white dashed) is calculated through the centroid method and the aperture is selected as the minimum circle, which contains all areas where $\varepsilon \geq \varepsilon_{\max}/e^2$. Here, e and $\varepsilon_{\max}$ represent the natural constant and maximum energy density, respectively. Corresponding, the reconstructed $\Delta\Phi$ is shown in Fig. 2(c) and the obvious defocusing term (convex wave-front) due to curved plasma mirrors matches our expectation.

To further verify the validity of our wave-front reconstruction algorithm, the intensity distributions of tenth harmonics on the y-t and z-t plane, which are emitted from the peak incident cycle, are illustrated in Figs. 3(a) and 3(b), respectively. Clearly, distorted wave-fronts indicate the existence of various aberrations. Both planes contain the aperture center (y_c, z_c). The white dashed lines
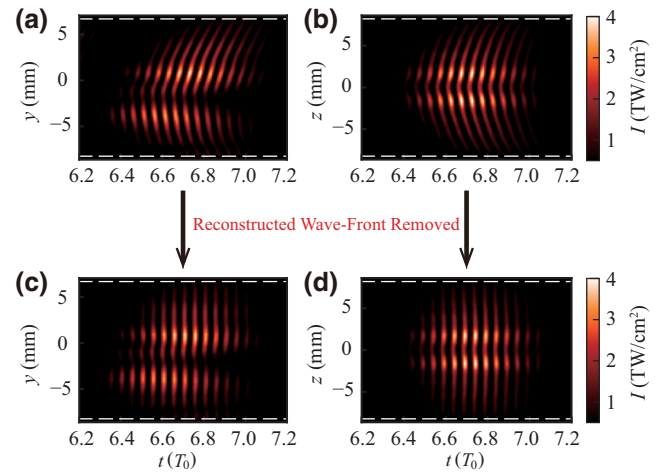

FIG. 3. (a),(b) The far-field intensity distribution of tenth harmonics on y-t plane ($z = z_c \approx 0$ mm) and z-t plane ($y = y_c \approx -1$ mm), respectively, where (y_c, z_c) represent the coordinate of the centroid shown in Fig. 2(b). Edges of the aperture are shown by the white dashed line. (c),(d) Corresponding intensity distributions with reconstructed wave-fronts that are illustrated in Fig. 2(c) removed.

represent edges of the aperture. However, as shown in Figs. 3(c) and 3(d), flatter distributions are obtained after removing the distortion shown in (a)–(b) by reconstructed $\Delta\Phi$ illustrated in Fig. 2(c), which confirm that our method is suitable for the aberration analysis in RHHG. The remaining small distortion comes from the reality that the θ_y and θ_z used by our method are weighted average values calculated from time-varying wave-fronts of harmonics and the best-fitted wave-front for the whole attosecond trains is obtained. The wave-fronts, which change among different attosecond pulses, will be further discussed in our future works.

Then, the Zernike polynomial expansion result of Fig. 2(c) is illustrated in Fig. 4(a). Consistent with our expectation, only terms satisfying $Z_j(y, z, \rho) = Z_j(y, -z, \rho)$ are significant due to the symmetry. We note that the piston term Z_0 is a constant among C and does not introduce real influence. Utilizing Eqs. (4)–(7), we have $\Delta z \approx 1.74$ nm, $\Delta y \approx -0.37$ μm, $\Delta x \approx 16.8$ μm and $b_A \approx 0.42$ μm. Further, Fig. 4(b) illustrates the $\Delta x/5$ (red solid), Δy (blue solid), Δz (green solid), and b_A (orange solid) for different-order harmonics calculated from Eqs. (4)–(7). For all harmonics, the simulation values of Δz and Δx are close to our theoretical predictions, which are 0 and 17.7 μm, respectively. Here, the theoretical results of Δx (black dashed) is the theoretical maximum $-R_r = w_L^2 / 4L \cos\alpha$ obtained from Eq. (2). More simulations [shown in Figs. 4(d) and 4(e)] prove that the Δx, which is decoded from wave-fronts of harmonics, changes with varying α and keeps stable for different incident carrier-envelope phases ϕ_{CEP}, as expected by the theoretical analysis. Clearly, the deformation of the optical-curved
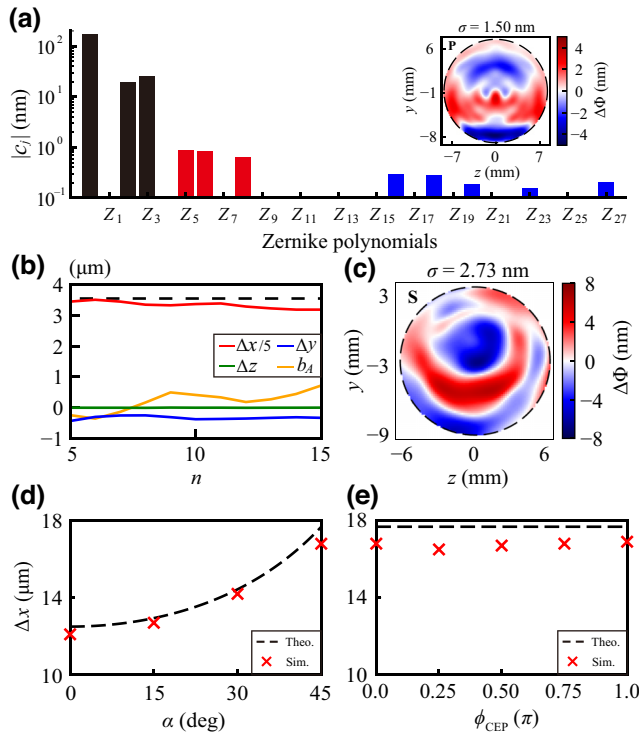
FIG. 4. (a) The Zernike polynomial decomposition result of the wave-front shown in Fig. 2(c) where the p-polarized incident laser used. Here, high-order aberrations (orders of polynomial > 10) are marked by blue and low-order aberrations ($Z_4 - Z_{10}$) are marked by red. The inset illustrates the aberration distribution without $Z_0 - Z_3$ (black blocks). (b) $\Delta x/5$ (red solid), Δy (blue solid), Δz (green solid), and b_A (orange solid) for 5–15th harmonics. (c) Reconstructed $\Delta \Phi$ ($Z_0 - Z_3$ terms removed) for tenth harmonics, which are generated from the s-polarized incident laser. (d) Simulation results (red crosses) and theoretical predictions (black dashed) of Δx for tenth harmonics generated from p-polarized incident lasers with varying α. (e) Similar to (d) but for different ϕ_{CEP}.

plasma mirror, which is impacted by α significantly, greatly influences the properties of far-field wave-fronts of harmonics. Besides, the rarely changed negative Δy indicates that all harmonics are emitted from the same place before the plasma bulk, which is the property of relativistic oscillating mirror mechanism [7]. We note that the $b_A \ll \Delta x$ is also consistent with our expectation Eq. (2), whose small value may originate from the change of the curvature radii of plasma mirrors due to the instability of interactions.

Removing the Zernike terms $Z_0 - Z_3$ that do not affect the imaging quality of beams after refocusing [28], we obtain the aberration distributions shown in the inset of Fig. 4(a), which is symmetric about the z axis with $\sigma \sim 1.50$ nm and peak to valley (PV) approximately 8 nm. As illustrated in Fig. 4(a), the main aberrations contained in the inset are vertical primary astigmatism (Z_5), coma (Z_6), and oblique coma (trefoil, Z_8) while other high-order
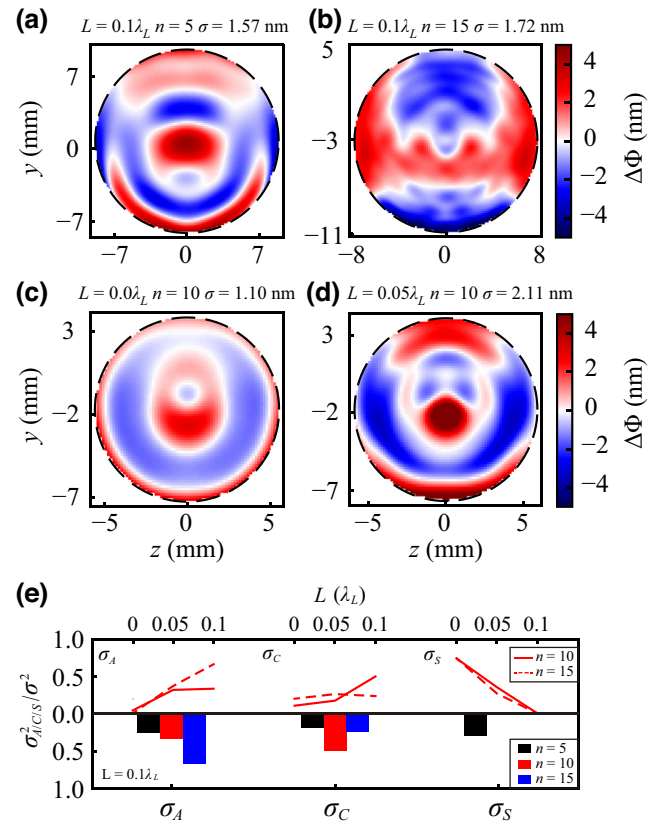

FIG. 5. Far-field aberration distributions ($Z_0 - Z_3$ removed) of fifth (a) and 15th (b) harmonics where $L = 0.1\lambda_L$ and $x_{i0} = 0$. (c),(d) Similarly, but for tenth harmonics where $L = 0.0\lambda_L$ and $0.05\lambda_L$, respectively. (e) For different preplasma scales (top half) and orders of harmonics (bottom half), the contribution proportion $\sigma_{A/C/S}^2/\sigma^2$ of different aberration types in $\Delta \Phi$ whose $Z_0 - Z_3$ terms are removed.

aberrations (blue bar) contributes to complex details of the wave-front. Further, with a s-polarized incident laser used, we show the wave-front of tenth harmonics without the contribution of $Z_0 - Z_3$ terms in Fig. 4(c). Due to the break of the symmetric setting, the aberration distribution loses the symmetry either and becomes more complicated with higher values of $\sigma \sim 2.73$ nm and PV ~ 13 nm.

In Fig. 5, the aberration distributions without $Z_0 - Z_3$ terms of different-order harmonics [(a) fifth and (b) 15th harmonics] generated from targets where $L = 0.1\lambda_L$ and tenth harmonics with different preplasma scale [(c) $L = 0.0\lambda_L$ and (d) $0.05\lambda_L$] used are illustrated. While distributions are different for different cases, all patterns are symmetric about the z axis due to p-polarized incident lasers and keep stable nanoscale σ. The contribution proportions ($\sigma_{A/C/S}^2/\sigma^2$) of the aberration terms associated with astigmatism (σ_A), coma (σ_C) and spherical aberration (σ_S) are shown in Fig. 5(e), which vary with the preplasma scale L (top half) and harmonic frequencies (bottom half). Here, with L changing from 0 to $0.1\lambda_0$, the solid and dashed
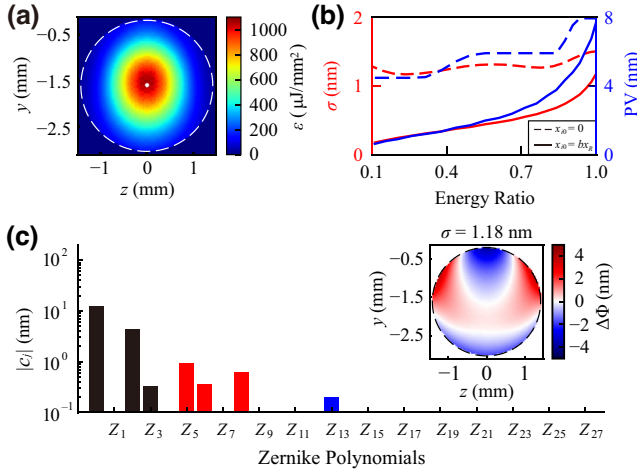
(a) **(b)** **(c)**

(c)

FIG. 6. (a) Similar to Fig. 2(b), far-field energy distribution ε ($x_{\text{far}} = 10^5 \lambda_L$) of reflected tenth harmonics but for defocusing setting where $x_{i0} = b x_R \approx -14 \, \mu m$. Here, $b \equiv -4\pi L \cos \alpha / \lambda_L$. (b) Comparison for σ (red) and PV (blue) of aberration distributions of tenth harmonics obtained from focusing (dashed) and defocusing (solid) setting. Here, contributions of $Z_0 - Z_3$ are removed. (c) Similar to Fig. 4(a) but for $x_{i0} \approx -14 \, \mu m$.

red lines illustrate results obtained from cases where $n = 10$ and $n = 15$, respectively. Besides, the black, red, and blue blocks represent the values for $n = 5$, 10, and 15 when $L = 0.1\lambda_L$, respectively. On the one hand, these three types are the major aberrations as they contribute more than 80% σ^2 for all cases. On the other hand, the spherical aberration is significant for low-order harmonics and short preplasma scale where the plasma mirror can not be well approximated to a parabolic one, especially for $L = 0.0\lambda_L$. However, with the increase of n or L, coma and astigmatism become significant. When $n = 15$, $L = 0.1\lambda_L$, astigmatism is the dominant one due to the increased instability where $(\sigma_A/\sigma)^2 > 60\%$. Similar trends are observed in more simulations, which are not shown here for brevity. The comprehensive elucidation is to be furnished in the forthcoming work.

In our recent work [17,18], we have shown that a proper defocusing incident laser whose $x_{i0} = -4\pi L x_R \cos \alpha / \lambda_L$ can generate higher-quality far-field attosecond pulses with higher near-axis intensity and lower divergences as the focusing effect of optically curved plasma mirrors is offset. Such advantages are also confirmed in Fig. 6(a), where the far-field energy density distribution ε of tenth harmonics generated from the incident laser with optimal defocusing distance ($x_{i0} \approx -14 \, \mu m$) is illustrated. Comparing to Fig. 2(b) where the same parameters are used except $x_{i0} = 0$, not only is compacter spot obtained with $\varepsilon_{\max}$ improved about 17 times, but also the Gaussian-like distribution is generated in the defocusing situation. Moreover, the quality of wave-fronts is also improved as illustrated in Fig. 6(c). The greatly reduced Z_3 term
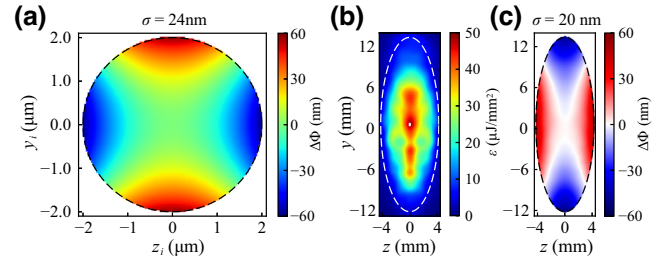

FIG. 7. (a) The incident distorted wave-front with astigmatism. (b) The far-field energy density distribution of the tenth harmonics. (c) The far-field aberration distribution ($Z_0 - Z_3$ terms removed) of the tenth harmonics. The elliptical aperture (white and black dashed) is chosen for accurate analysis.

indicates that the defocusing setting works and $|\Delta x|$ closes to zero as expected. At the same time, the σ of aberration pattern without $Z_0 \sim Z_3$ terms [inset of Fig. 6(c)] decreases to 1.18 nm and Z_j terms higher than Z_{13} disappear, which results in more regular wave-front distribution. Of note, if we decrease the size of apertures, as shown in Fig. 6(b), the values of σ (red), and PV (blue) of aberration distributions obtained in the defocusing situation (solid lines) are suppressed significantly, which improves slowly if focusing incident lasers are utilized (dashed lines). The significantly improved spot and wave-fronts prove that a proper defocusing incident laser benefits the generation of brilliant aberration-free attosecond pulses. They are crucial for practical applications where transmission and refocusing of pulses are required and such pulses can be further improved with minor compromise of pulse energy.

Furthermore, the influence of the incident aberration on reflected harmonics is illustrated in Fig. 7. As shown in Fig. 7(a), the astigmatism term Z_5 ($\sigma = 0.03\lambda_L = 24$ nm) is added to the wave-front of the incident laser at its focus. Irradiating the plasma target when $\alpha = \pi/4$ and $x_{i0} = 0$, the beam generates a distorted relativistic plasma mirror. According to Eqs. (B2)–(B6), due to the different incident curvature radii R_i and focal lengths of the plasma mirror on tangential and sagittal planes, the reflected harmonics also have different curvature radii on these two orthogonal planes. Verified by Figs. 7(b) and 7(c), the elliptical far-field energy-density distribution and significant astigmatism aberration ($\sigma \approx 20$ nm) of the tenth harmonic are obtained, respectively, where the ratio between the major and minor axis of the aperture (white and black dashed) is about 3.

IV. CONCLUSION AND DISCUSSION

In summary, we have proposed an alternative numerical method to reconstruct wave-fronts by extracting local propagation directions of beams from their complex electromagnetic field distributions. With the help of a currently developed algorithm, complete far-field wave-fronts of

harmonics emitted through RHHG have been successfully retrieved and the encoded information on optical properties and plasma features are analyzed.

Theoretical and numerical study shows that the foci of harmonics can be decoded from the tilt and defocusing terms of wave-fronts, giving rise to unveil the generation mechanism and optical properties of harmonics. As the increase of harmonic orders and preplasma scale, we have observed that the dominant wave-front distortions introduced by relativistic plasma surfaces transfer from spherical aberration to astigmatism. Consistent with our theory, the spatial properties of driving lasers and structures of optically curved plasma surfaces are decisive to the beam quality of the RHHG pulses. First of all, the wave-fronts of harmonics maintain symmetric with respect to polarization planes of p-polarized driving fields. Secondly, proper defocusing incident lasers ($x_{i0} = -4\pi L x_R \cos\alpha/\lambda_L$) can generate aberration-free XUV harmonics ($\sigma < 1$ nm and $> 80\%$ energy preserved) with Gaussian-like energy density (17 times increase compared to focusing setting) distribution. Last but not least, harmonics with elliptical intensity distribution are observed when the driving laser has initial astigmatism aberration, which is further regulated by the plasma surfaces and well inherited by harmonics.

Present work provides an effective angle of view to understand the wave-fronts of harmonics from RHHG and a powerful tool to further optimize them, paving the way towards aberration-free XUV attosecond sources. Such beams are crucial for the metrology and utilization of attosecond pulses, especially for applications in strong field interactions [37], multiphoton ionization [38], barrier suppression ionization [39] as well as nonlinear cluster interactions [40]. Moreover, our reconstruction method can be further used on numerical investigations of other radiation sources such as gaseous high-order harmonic generation [41], x-ray free-electron lasers [42], and terahertz radiation [43]. While not presented for clarity, our reconstruction method is rather robust for an extensive range of laser-plasma interaction conditions, including the incident intensity and plasma density. Further, in combination with short-time Fourier transformation, the temporal evolution of wave-fronts can also be resolved, giving access to study spatiotemporal coupling for tightly focused, few-cycle or vortex beams. It is also worthwhile to note that our algorithm can also be used to retrieve the near-field wave-front from PIC simulation results, which is few discussed here as the practical metrology and applications are normally performed in the far field and the propagation effects can greatly modify its properties.

APPENDIX A: WAVE-FRONT RECONSTRUCTION ALGORITHM

According to the definition of $\Delta\Phi$ explained in Fig. 1, $E(y, z, t)$ of the beam, which passes through the green
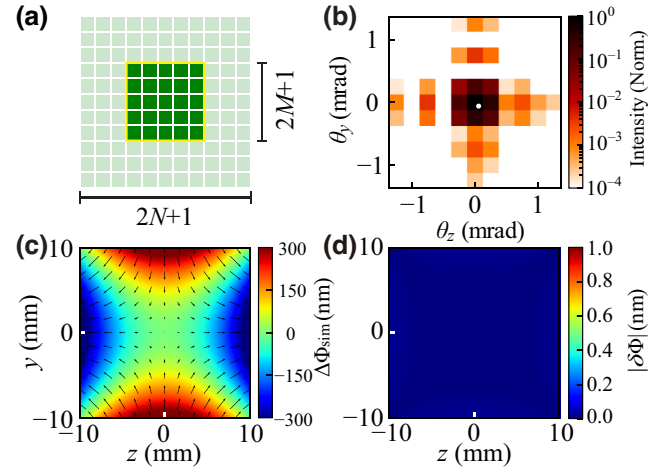

FIG. 8. (a) The schematic of the spatial window with $(2N+1)^2$ grids where central $(2M+1)^2$ dark green grids represent the area with real field information and others represent the artificial zero zone. (b) The spectrum (background) and transverse propagation directions (white point) of the local incident electric field selected by the spatial window, whose geometric center is set as the black point illustrated in Fig. 1. (c) The reconstructed $\Delta\Phi_{sim}$ (background) and local transverse propagation directions (black arrows) of the incident beam shown in Fig. 1. (d) The difference $|\delta\Phi|$ between the reconstructed $\Delta\Phi_{sim}$ and the real $\Delta\Phi$.

screen normally, can be expressed as

$$E(y, z, t) = E_0(t) \exp\left[-i\omega_0 t - ik_0 \Delta\Phi(y, z)\right], \quad \text{(A1)}$$

where $E_0(t)$, ω_0, $k_0 \equiv 2\pi/\lambda_0$, and λ_0 represent the amplitude with Gaussian temporal envelope, angular frequency, wave number, and wavelength of the beam, respectively. As a benchmark, we set $\Delta\Phi$ as $\Delta\Phi(y, z) = 400 \times \left[(y/y_L)^2 - (z/z_L)^2\right]$ nm in Fig. 1, where $y_L = z_L = 10$ mm.

As discussed in the text, the square spatial window $W(y, z)$ (yellow square in Fig. 1) is utilized in our method to choose small analysis areas from the whole wave-front. Shown in Fig. 8(a), the spatial window contains $(2M+1)^2$ spatial grids with real field information (dark green squares). The side length of each grid $\Delta s = 200\lambda_0$ and $\lambda_0 = 1\,\mu$m. Besides, extra zero zones (light green squares) are added and extend the side length of the window to $(2N+1)\Delta s$, i.e., containing $(2N+1)^2$ grids. Therefore, the mathematical formula of $W(y, z)$ can be expressed as

$$W(y, z) = w(y) \times w(z) \quad \text{(A2)}$$

$$w(y) = \begin{cases} 1, & |y| \leq M\Delta s \\ 0, & \text{else}, \end{cases} \quad \text{(A3)}$$

where the zero point is set as the center of the square window. In this paper, we choose $M = 2$ and $N = 5$ for all simulations.

Without loss of generality, we consider the complex amplitude U of electric fields around the zero point $(0, 0)$. Utilizing Taylor series, it can be approximated as

$$U(y, z) = E_0 W \exp\left[ik_y^c y + ik_z^c z - ik_0 \Delta\Phi(0, 0)\right], \quad \text{(A4)}$$

where $(k_y^c, k_z^c) \equiv -k_0 \nabla(\Delta\Phi)$ are transverse wave vectors and φ_0 is a constant. Here, the wave-front of local electromagnetic field is approximately flat. After propagating a distance x_p where the Fraunhofer approximation [44] is satisfied, we obtain the corresponding far-field complex amplitude $\widetilde{U}$:

$$\widetilde{U}(\xi, \zeta) \propto \iint_{-\infty}^{+\infty} U \exp\left[-i\frac{k_0}{x_p}(y\xi + z\zeta)\right] dy\, dz, \quad \text{(A5)}$$

where ξ and ζ represent spatial coordinates on two orthogonal axes that meet in point $(x_p, 0, 0)$ and are parallel to y and z axes, respectively.

Defining $k_y \equiv k_0 \xi / x_p$ and $k_z \equiv k_0 \zeta / x_p$, we find the intensity distribution of diffraction pattern $\|\widetilde{U}(\xi, \zeta)\|^2$, which is characterized by Hartmann wave-front sensors at the plane $x = x_p$ is actually the spectra distribution $\|\widetilde{U}(k_y, k_z)\|^2$ of $U(y, z)$ at the plane $x = 0$. Therefore, similar to the first-order centroid methods used in experiments, we can use Eqs. (A6)–(A7) to calculate the transverse propagation directions of fields from spectra, i.e., $\theta_y \equiv k_y^c / k_0$ and $\theta_z \equiv k_z^c / k_0$.

$$\theta_y = \frac{\iint_{-\infty}^{+\infty} k_y \|\widetilde{U}(k_y, k_z)\|^2 dk_y\, dk_z}{k_0 \iint_{-\infty}^{+\infty} \|\widetilde{U}(k_y, k_z)\|^2 dk_y\, dk_z}, \quad \text{(A6)}$$

$$\theta_z = \frac{\iint_{-\infty}^{+\infty} k_z \|\widetilde{U}(k_y, k_z)\|^2 dk_y\, dk_z}{k_0 \iint_{-\infty}^{+\infty} \|\widetilde{U}(k_y, k_z)\|^2 dk_y\, dk_z}. \quad \text{(A7)}$$

Numerically, discrete Fourier transformation (DFT) is used for the calculation of spectra. Therefore, we have the DFT result of Eq. (A4) after derivation:

$$\widetilde{U}(k_y^j, k_z^j) \propto \widetilde{u}(k_y^j) \times \widetilde{u}(k_z^j), \quad \text{(A8)}$$

$$\widetilde{u}(k^j) = \sum_{n=-N}^{N} \mathrm{w}(n\Delta s) \exp\left[-i(k^j - k^c)n\Delta s\right], \quad \text{(A9)}$$

where $k^j = 2\pi j / (2N + 1)\Delta s, j = 0, \pm1, \pm2, \ldots, \pm N$. The spatial subscripts in Eq. (A9) and derivations below are neglected because of the symmetry. Using Eq. (A3), we have

$$\widetilde{u}(k^j) = 1 + 2\sum_{n=1}^{M} \cos\left[n(k^j - k^c)\Delta s\right],$$

$$= \frac{\sin\left[(M + \frac{1}{2})(k^j - k^c)\Delta s\right]}{\sin\left[\frac{1}{2}(k^j - k^c)\Delta s\right]}. \quad \text{(A10)}$$
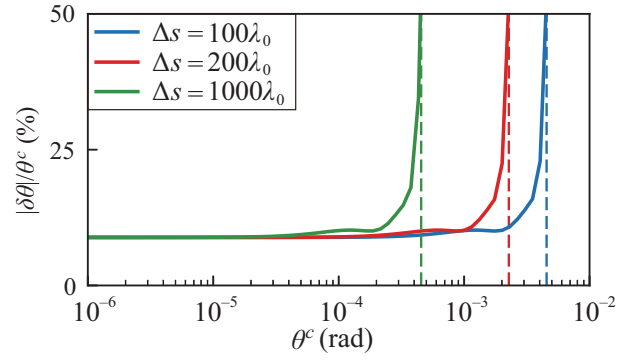

FIG. 9. The relative calculation error $|\delta\theta|/\theta^c$ for varying θ^c when $M = 2$ and $N = 5$. The blue, red, and green lines represent the results when Δs equals $100\lambda_0$, $200\lambda_0$, and $300\lambda_0$, respectively.

Further, according to Eqs. (A6)–(A7), we obtain the calculation error of propagation directions $\delta\theta$ as

$$\delta\theta = \frac{\sum_{j=-N}^{N} k^j \|\widetilde{u}(k^j)\|^2}{k_0 \sum_{j=-N}^{N} \|\widetilde{u}(k^j)\|^2} - \frac{k^c}{k_0}. \quad \text{(A11)}$$

Here, the integration in Eqs. (A6)–(A7) is transformed to summation. Clearly, $\delta\theta$ depends on the the value of M, N, and Δs. As illustrated in Fig. 9 where $M = 2$ and $N = 5$, our reconstruction method only fails when θ^c is close to the limitation of Fourier transformation $\theta_{\max}^c \approx \lambda_0 / 2\Delta s$ (colorful dashed). And when θ^c is small, the ratio between $\delta\theta$ and θ^c remains stable. To reconstruct the wave-front accurately, $\delta\theta$ is calculated and offset in our algorithm, automatically.

For instance, the spectrum of fields around the black point in Fig. 1 is illustrated in Fig. 8(b) and the white point indicates the local (θ_y, θ_z). Moving the spatial window and utilizing Eqs. (A6)–(A7), as shown in Fig. 8(c), the distribution of θ_y and θ_z (black arrows) among the whole wave-front is obtained. Finally, the wave-front $\Delta\Phi_{\text{sim}}$ [Fig. 8(c)] is reconstructed from its gradient field, which is represented by $-\theta_y$ and $-\theta_z$, through the well-known Southwell method [45]. As illustrated in Fig. 1(e), the absolute value of reconstruction error $\delta\Phi \equiv \Delta\Phi - \Delta\Phi_{\text{sim}}$ is negligible, confirming the validity of our algorithm. It is deserved to note that, for more complex electromagnetic fields with time-varying wave-fronts, the $\Delta\Phi_{\text{sim}}$ obtained from our method is actually a weighted average one as the centroid method is used. Besides, as the θ^c of the reconstructed wave-fronts in our paper is only in 10^{-6} rad scale ($\Delta s = 200\lambda_L$), which are generated from smooth plasma surfaces, our method is capable of dealing with the situation where rough surfaces are set.

APPENDIX B: INFLUENCE OF PLASMA MIRRORS ON WAVE-FRONTS OF REFLECTED HARMONICS

Considering the refocused Gaussian-like nth harmonic emitted from optically curved plasma mirrors in RHHG, its q parameters [46] on the plasma mirror and in the far field ($x = x_{\text{far}}$) are defined as $q_{sn}^{-1} \equiv R_r^{-1} - i\lambda_L/n\pi w_{sn}^2$ and $q_{fn}^{-1} \equiv R_{fn}^{-1} - i\lambda_L/n\pi w_{fn}^2$, respectively. Here, w_{sn} and w_{fn} represent corresponding local transverse spatial radii of beams. Besides, R_r and R_{fn} represents local curvature radii of beams. Utilizing the relationship $q_{fn} = q_{sn} + x_{\text{far}}$ [46], we obtain

$$
\begin{aligned}
R_{fn} &= x_{\text{far}} + \frac{R_r}{1 + h_n^2} \left[1 + \frac{h_n^2}{1 + (1 + h_n^2)x_{\text{far}}/R_r} \right] \\
&\approx x_{\text{far}} + R_r \left(1 + h_n^2 \right)^{-1},
\end{aligned} \tag{B1}
$$

where $h_n \equiv \lambda_L R_r/n\pi w_{sn}^2$ and the far-field assumption $x_{\text{far}} \gg n\pi w_{sn}^2/\lambda_L$ is used.

According to Ref. [29], due to the focusing effect of curved plasma mirrors, the R_r satisfies

$$
1/R_i^t - 1/R_r^t = 1/f_p^t \cos\alpha \tag{B2}
$$

$$
1/R_i^s - 1/R_r^s = \cos\alpha/f_p^s \tag{B3}
$$

where R_i and f_p represent the curvature radii of incident lasers on plasma mirrors and the focusing length of the plasma mirror, respectively. Here, superscripts t and s mark the corresponding values on tangential ($z = 0$) and sagittal ($y = 0$) planes. According to Eq. (B1), due to the difference between R_{fn} and the curvature radius $R_{\text{ref}} = x_{\text{far}}$ of the reference spherical wave-front, we obtain the quadratic term of $\Delta\Phi$ as $\left(R_r^t H_n^t y^2 + R_r^s H_n^s z^2 \right)/2x_{\text{far}}^2$, where $H_n \equiv (1 + h_n^2)^{-1}$. Here, the symmetric setting with p-polarized incident lasers used is assumed. Therefore, adding the constant and linear terms discussed in the text, we obtain the theoretical wave-fronts of nth reflected harmonics in the far field as

$$
\begin{aligned}
\Delta\Phi &\approx \Phi_0 + \frac{\Delta y}{x_{\text{far}}} y + \frac{R_r^s H_n^s + R_r^t H_n^t}{4x_{\text{far}}^2} \left(z^2 + y^2 \right) \\
&\quad + \frac{R_r^s H_n^s - R_r^t H_n^t}{4x_{\text{far}}^2} \left(z^2 - y^2 \right).
\end{aligned} \tag{B4}
$$

We note that the longitudinal movement of foci Δx is introduced by the defocusing term [the third term in Eq. (B4)] and satisfies $\Delta x = -\frac{1}{2} \left(R_r^s H_n^s + R_r^t H_n^t \right)$ [28].

Specifically, according to Ref. [11], for a Gaussian incident beam without initial aberration, we have the focusing length f_p^t and f_p^s as

$$
f_p^t = w_s^2(1 + \epsilon^{-1})/4L \cos^2\alpha, \tag{B5}
$$

$$
f_p^s = w_s^2(1 + \epsilon^{-1})/4L, \tag{B6}
$$

where $\epsilon^{-1} \equiv \pi L/a_L\lambda_L(1 - \sin\alpha)$ characterizes the impact of laser intensity on the shape of plasma mirrors and is negligible if the normalized peak amplitude $a_L \gg 1$. Here, $w_s = w_L\sqrt{1 + (x_{i0}/x_R)^2}$ is the radius of the incident laser on the plasma mirror. We note that the appearance of $1/\cos^2\alpha$ in f_p^t stems from the projection of w_s on the target. Therefore, combining with Eqs. (B2)–(B3), we have

$$
R_r^s = R_r^t = -\frac{x_{i0}^2 + x_R^2}{x_{i0} + 4\pi L x_R \cos\alpha/\lambda_L(1 + \epsilon^{-1})}. \tag{B7}
$$

As a result, the coefficient of $z^2 - y^2$ is 0 in this situation.

APPENDIX C: ZERNIKE POLYNOMIALS

The Zernike polynomials $Z_j(y, z, \rho)$ used in this paper are defined as Eqs. (C1)–(C28) [31] and illustrated in Fig. 10, where $y' \equiv y/\rho$, $z' \equiv z/\rho$, and $\rho' \equiv \sqrt{y'^2 + z'^2} \in [0, 1]$. The polynomial terms represent aberrations including piston (Z_0), tilt ($Z_1 - Z_2$), defocusing (Z_3), primary astigmatism ($Z_4 - Z_5$), primary coma ($Z_6 - Z_7$), primary trefoil (elliptical coma, $Z_8 - Z_9$), primary spherical aberration (Z_{10}), secondary astigmatism ($Z_{11} - Z_{12}$), tetrafoil ($Z_{13} - Z_{14}$), secondary coma ($Z_{15} - Z_{16}$), secondary spherical aberration (Z_{21}), and tertius astigmatism ($Z_{22} - Z_{23}$), et al.

$$
Z_0 = 1, \tag{C1}
$$

$$
Z_1 = 2z', \tag{C2}
$$

$$
Z_2 = 2y', \tag{C3}
$$

$$
Z_3 = \sqrt{3}(2\rho'^2 - 1), \tag{C4}
$$

$$
Z_4 = 2\sqrt{6}y'z', \tag{C5}
$$

$$
Z_5 = \sqrt{6}(z'^2 - y'^2), \tag{C6}
$$

$$
Z_6 = \sqrt{8}(3\rho'^2 - 2)y', \tag{C7}
$$

$$
Z_7 = \sqrt{8}(3\rho'^2 - 2)z', \tag{C8}
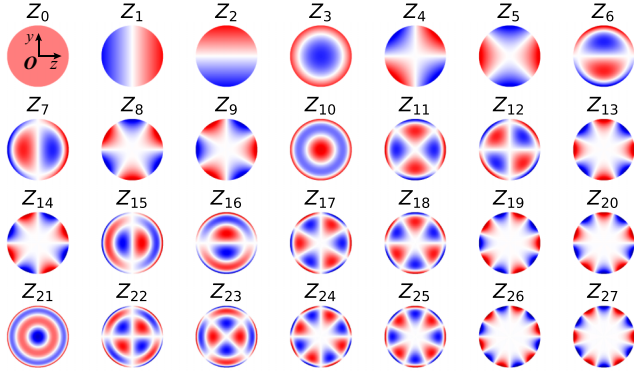$$

$$
Z_8 = \sqrt{8}(3z'^2 - y'^2)y', \tag{C9}
$$

FIG. 10. The Zernike polynomials from Z_0 to Z_{27} within a unit circle.

$$Z_9 = \sqrt{8}(z'^2 - 3y'^2)z', \tag{C10}$$

$$Z_{10} = \sqrt{5}(6\rho'^4 - 6\rho'^2 + 1), \tag{C11}$$

$$Z_{11} = \sqrt{10}(z'^2 - y'^2)(4\rho'^2 - 3), \tag{C12}$$

$$Z_{12} = 2\sqrt{10}(4\rho'^2 - 3)y'z', \tag{C13}$$

$$Z_{13} = \sqrt{10}(\rho'^4 - 8y'^2z'^2), \tag{C14}$$

$$Z_{14} = 4\sqrt{10}(z'^2 - y'^2)y'z', \tag{C15}$$

$$Z_{15} = \sqrt{12}(10\rho'^4 - 12\rho'^2 + 3)z', \tag{C16}$$

$$Z_{16} = \sqrt{12}(10\rho'^4 - 12\rho'^2 + 3)y', \tag{C17}$$

$$Z_{17} = \sqrt{12}(z'^2 - 3y'^2)(5\rho'^2 - 4)z', \tag{C18}$$

$$Z_{18} = \sqrt{12}(3z'^2 - y'^2)(5\rho'^2 - 4)y', \tag{C19}$$

$$Z_{19} = \sqrt{12}(16z'^4 - 20z'^2\rho'^2 + 5\rho'^4)z', \tag{C20}$$

$$Z_{20} = \sqrt{12}(16y'^4 - 20y'^2\rho'^2 + 5\rho'^4)y', \tag{C21}$$

$$Z_{21} = \sqrt{7}(20\rho'^6 - 30\rho'^4 + 12\rho'^2 - 1), \tag{C22}$$

$$Z_{22} = 2\sqrt{14}(15\rho'^4 - 20\rho'^2 + 6)y'z', \tag{C23}$$

$$Z_{23} = \sqrt{14}(z'^2 - y'^2)(15\rho'^4 - 20\rho'^2 + 6), \tag{C24}$$

$$Z_{24} = 4\sqrt{14}(z'^2 - y'^2)(6\rho'^2 - 5)y'z', \tag{C25}$$

$$Z_{25} = \sqrt{14}(8z'^4 - 8z'^2\rho'^2 + \rho'^4)(6\rho'^2 - 5), \tag{C26}$$

$$Z_{26} = \sqrt{14}(32z'^4 - 32z'^2\rho'^2 + 6\rho'^4)y'z', \tag{C27}$$

$$Z_{27} = \sqrt{14}(32z'^6 - 48z'^4\rho'^2 + 18z'^2\rho'^4 - \rho'^6). \tag{C28}$$

APPENDIX D: INFLUENCE OF THE ION MOVEMENT

The effect of ion motions on the plasma denting can be represented by a coefficient g [11], which equals 1 for fixed ions and modifies the focusing length of the plasma mirror
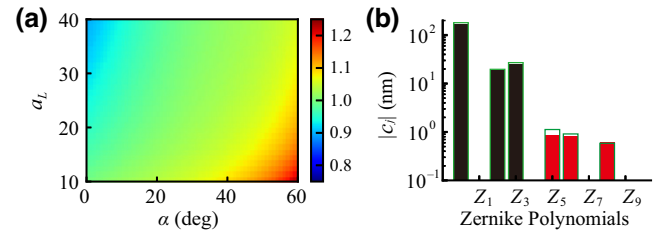

FIG. 11. (a) The value of coefficient g for different incident angle α and normalized amplitude of peak electric field strength a_L at the plasma mirror when $L = 0.1\lambda_L$. (b) The Zernike polynomial decomposition result of the far-field wave-front of the tenth harmonics with fixed (solid colorful bars) or mobile (hollow green bars) ions used.

as $f_p^t \approx w_s^2 g/4L \cos^2 \alpha$ and $f_p^s \approx w_s^2 g/4L$. Specifically, g is defined as

$$g = \frac{\epsilon + (1 + \mu\epsilon)^2}{\epsilon + 2\mu\epsilon(1 + \mu\epsilon)}, \tag{D1}$$

$$\mu = \frac{\omega_L(1 - \sin \alpha)\Pi_0}{4} \int_{-\infty}^{t} \frac{a_L(t_0)}{a_L(t = t_{max})} dt_0. \tag{D2}$$

We note that $\Pi_0 \equiv \sqrt{RZm_e \cos \alpha/2AM_p}$ where M_p represents the proton mass and the coefficient ϵ is defined in Appendix B. Considering that the g varies slowly around the time t_{max} [11] when the laser pulse reaches its peak intensity and harmonics are generated most efficiently, the wave-fronts of reflected harmonics are dominated by the value of $g = g(t = t_{max})$.

As illustrated in Fig. 11(a), $g(t = t_{max}) \sim 1$ across a broad parameter range, which encompasses varying peak electric field intensity (represented by the normalized amplitude a_L) and incident angle α. Here, the plasma reflection coefficient $R = 0.7$, the average charge state $Z = 6$ and the mass number of the ions $A = 12$ are used. Due to such a parameter range containing the considered scenario in the main text, regardless of the utilization of fixed (solid colorful bars) or movable (hollow green bars) ions, the Zernike polynomial decomposition results of the tenth reflected far-field wave-fronts remain almost unchanged for the simulation setting used in Fig. 2, as shown in Fig. 11(b). Therefore, it is rational to neglect the motion of ions in the simulations.

[1] F. Krausz and M. Ivanov, Attosecond physics, Rev. Mod. Phys. **81,** 163 (2009).

[2] S. X. Hu and L. A. Collins, Attosecond pump probe: Exploring ultrafast electron motion inside an atom, Phys. Rev. Lett. **96,** 073004 (2006).

[3] F. Lépine, M. Y. Ivanov, and M. J. J. Vrakking, Attosecond molecular dynamics: fact or fiction?, Nat. Photonics **8,** 195 (2014).

[4] A. L. Cavalieri, N. Müller, T. Uphues, V. S. Yakovlev, A. Baltuška, B. Horvath, B. Schmidt, L. Blümel, R. Holzwarth, S. Hendel, *et al.*, Attosecond spectroscopy in condensed matter, Nature **449,** 1029 (2007).

[5] J. Meyer-ter Vehn, J. Honrubia, M. Geissler, S. Karsch, F. Krausz, G. Tsakiris, and K. Witte, On electron transport in fast ignition research and the use of few-cycle pw-range laser pulses, Plasma Phys. Control. Fusion **47,** B807 (2005).

[6] A. Sundström, M. Grech, I. Pusztai, and C. Riconda, Stimulated-Raman-scattering amplification of attosecond XUV pulses with pulse-train pumps and application to local in-depth plasma-density measurement, Phys. Rev. E **106,** 045208 (2022).

[7] T. Baeva, S. Gordienko, and A. Pukhov, Theory of high-order harmonic generation in relativistic laser interaction with overdense plasma, Phys. Rev. E **74,** 046404 (2006).

[8] D. an der Brügge and A. Pukhov, Enhanced relativistic harmonics by electron nanobunching, Phys. Plasmas **17,** 033110 (2010).

[9] M. R. Edwards and J. M. Mikhailova, The x-ray emission effectiveness of plasma mirrors: Reexamining power-law scaling for relativistic high-order harmonic generation, Sci. Rep. **10,** 5154 (2020).

[10] U. Teubner and P. Gibbon, High-order harmonics from laser-irradiated plasma surfaces, Rev. Mod. Phys. **81,** 445 (2009).

[11] H. Vincenti, S. Monchocé, S. Kahaly, G. Bonnaud, P. Martin, and F. Quéré, Optical properties of relativistic plasma mirrors, Nat. Commun. **5,** 3403 (2014).

[12] F. Quéré, C. Thaury, J.-P. Geindre, G. Bonnaud, P. Monot, and P. Martin, Phase properties of laser high-order harmonics generated on plasma mirrors, Phys. Rev. Lett. **100,** 095004 (2008).

[13] A. Leblanc, S. Monchocé, H. Vincenti, S. Kahaly, J.-L. Vay, and F. Quéré, Spatial properties of high-order harmonic beams from plasma mirrors: A ptychographic study, Phys. Rev. Lett. **119,** 155001 (2017).

[14] H. Kallala, F. Quéré, and H. Vincenti, Techniques to generate intense isolated attosecond pulses from relativistic plasma mirrors, Phys. Rev. Res. **2,** 043007 (2020).

[15] L. Fedeli, A. Sainte-Marie, N. Zaim, M. Thévenet, J. L. Vay, A. Myers, F. Quéré, and H. Vincenti, Probing strong-field QED with doppler-boosted petawatt-class lasers, Phys. Rev. Lett. **127,** 114801 (2021).

[16] D. an der Brügge and A. Pukhov, Propagation of relativistic surface harmonics radiation in free space, Phys. Plasmas **14,** 093104 (2007).

[17] Y. Zhang, C. L. Zhong, S. P. Zhu, X. T. He, M. Zepf, and B. Qiao, Obtaining intense attosecond pulses in the far field from relativistic laser-plasma interactions, Phys. Rev. Appl. **16,** 024042 (2021).

[18] Y. Zhang, C. L. Zhong, S. P. Zhu, X. T. He, and B. Qiao, Divergence gating towards far-field isolated attosecond pulses, New J. Phys. **24,** 033038 (2022).

[19] H. Wikmark, C. Guo, J. Vogelsang, P. W. Smorenburg, H. Coudert-Alteirac, J. Lahl, J. Peschel, P. Rudawski, H. Dacasa, S. Carlström, *et al.*, Spatiotemporal coupling of attosecond pulses, Proc. Natl. Acad. Sci. U.S.A. **116,** 4779 (2019).

[20] C. Bourassin-Bouchet, M. M. Mang, F. Delmotte, P. Chavel, and S. de Rossi, How to focus an attosecond pulse, Opt. Express **21,** 2506 (2013).

[21] X. Ge, W. Boutu, D. Gauthier, F. Wang, A. Borta, B. Barbrel, M. Ducousso, A. I. Gonzalez, B. Carré, D. Guillaumet, M. Perdrix, O. Gobert, J. Gautier, G. Lambert, F. R. N. C. Maia, J. Hajdu, P. Zeitoun, and H. Merdji, Impact of wavefront and coherence optimization in coherent diffractive imaging, Opt. Express **21,** 11441 (2013).

[22] A. Leblanc, S. Monchocé, C. Bourassin-Bouchet, S. Kahaly, and F. Quéré, Ptychographic measurements of ultrahigh-intensity laser–plasma interactions, Nat. Phys. **12,** 301 (2016).

[23] P. Mercère, P. Zeitoun, M. Idir, S. Le Pape, D. Douillet, X. Levecq, G. Dovillaire, S. Bucourt, K. A. Goldberg, P. P. Naulleau, and S. Rekawa, Hartmann wave-front measurement at 13.4 nm with $\lambda_{EUV}/120$ accuracy, Opt. Lett. **28,** 1534 (2003).

[24] H. Dacasa, H. Coudert-Alteirac, C. Guo, E. Kueny, F. Campi, J. Lahl, J. Peschel, H. Wikmark, B. Major, E. Malm, *et al.*, Single-shot extreme-ultraviolet wavefront measurements of high-order harmonics, Opt. Express **27,** 2656 (2019).

[25] L. Li, Y. Wang, S. Wang, E. Oliva, L. Yin, T. T. Thuy Le, S. Daboussi, D. Ros, G. Maynard, S. Sebban, B. Hu, J. J. Rocca, and P. Zeitoun, Wavefront improvement in an injection-seeded soft x-ray laser based on a solid-target plasma amplifier, Opt. Lett. **38,** 4011 (2013).

[26] M. Ruiz-Lopez, M. Mehrjoo, B. Keitel, E. Plönjes, D. Alj, G. Dovillaire, L. Li, and P. Zeitoun, Wavefront sensing for evaluation of extreme ultraviolet microscopy, Sensors **20,** 6426 (2020). https://www.mdpi.com/1424-8220/20/22/6426

[27] L. Li, J. C. P. Koliyadu, H. Donnelly, D. Alj, O. Delmas, M. Ruiz-Lopez, O. de La Rochefoucauld, G. Dovillaire, M. Fajardo, C. T. Zhou, *et al.*, High numerical aperture Hartmann wave-front sensor for extreme ultraviolet spectral range, Opt. Lett. **45,** 4248 (2020).

[28] J. C. Wyant and K. Creath, *Basic Wavefront Aberration Theory for Optical Metrology*, Applied Optics and Optical Engineering Vol. 11 (Academic Press, Sab Diego, 1992).

[29] J. Turunen, Astigmatism in laser beam optical systems, Appl. Optics **25**, 2908 (1986).

[30] P. Arguijo and M. S. Scholl, Exact ray-trace beam for an off-axis paraboloid surface, Appl. Optics **42**, 3284 (2003).

[31] M. Bass, *Handbook of Optics: Volume II - Design, Fabrication, and Testing; Sources and Detectors; Radiometry and Photometry* (McGraw-Hill Education, New York, 2010), 3rd ed.

[32] K. Fuerschbach, J. P. Rolland, and K. P. Thompson, Theory of aberration fields for general optical systems with freeform surfaces, Opt. Express **22**, 26585 (2014).

[33] T. D. Arber, K. Bennett, C. S. Brady, A. Lawrence-Douglas, M. G. Ramsay, N. J. Sircombe, P. Gillies, R. G. Evans, H. Schmitz, A. R. Bell, *et al.*, Contemporary particle-in-cell approach to laser-plasma modelling, Plasma Phys. Control. Fusion **57**, 113001 (2015).

[34] A. Taflove and S. C. Hagness, *Computational Electrodynamics: The Finite-Difference Time-Domain Method* (Artech House, Boston, 2005), 3rd ed.

[35] N. M. Naumova, J. A. Nees, I. V. Sokolov, B. Hou, and G. A. Mourou, Relativistic generation of isolated attosecond pulses in a λ^3 focal volume, Phys. Rev. Lett. **92**, 063902 (2004).

[36] D. V. Vinogradov, Mirror conversion of Gaussian beams with simple astigmatism, Int. J. Infrared Milli. **16**, 1945 (1995).

[37] L. Gallmann, C. Cirelli, and U. Keller, Attosecond science: Recent highlights and future trends, Annu. Rev. Phys. Chem. **63**, 447 (2012).

[38] M. Kretschmar, A. Hadjipittas, B. Major, J. Tümmler, I. Will, T. Nagy, M. J. J. Vrakking, A. Emmanouili-dou, and B. Schütte, Attosecond investigation of extreme-ultraviolet multi-photon multi-electron ionization, Optica **9**, 639 (2022).

[39] I. Y. Kostyukov and A. A. Golovanov, Field ionization in short and extremely intense laser pulses, Phys. Rev. A **98**, 043407 (2018).

[40] T. Fennel, K.-H. Meiwes-Broer, J. Tiggesbäumker, P.-G. Reinhard, P. M. Dinh, and E. Suraud, Laser-driven nonlinear cluster dynamics, Rev. Mod. Phys. **82**, 1793 (2010).

[41] C. Winterfeldt, C. Spielmann, and G. Gerber, Colloquium: Optimal control of high-harmonic generation, Rev. Mod. Phys. **80**, 117 (2008).

[42] Y. W. Liu, M. Seaberg, D. L. Zhu, J. Krzywinski, F. Seiboth, C. Hardin, D. Cocco, A. Aquila, B. Nagler, H. J. Lee, *et al.*, High-accuracy wavefront sensing for x-ray free electron lasers, Optica **5**, 967 (2018).

[43] G. Q. Liao, Y. T. Li, C. Li, H. Liu, Y. H. Zhang, W. M. Jiang, X. H. Yuan, J. Nilsen, T. Ozaki, W. M. Wang, *et al.*, Intense terahertz radiation from relativistic laser–plasma interactions, Plasma Phys. Control. Fusion **59**, 014039 (2017).

[44] J. W. Goodman, *Introduction to Fourier Optics* (W. H. Freeman, New York, 2017), 4th ed.

[45] W. H. Southwell, Wave-front estimation from wave-front slope measurements, J. Opt. Soc. Am. **70**, 998 (1980).

[46] B. E. A. Saleh and M. C. Teich, *Fundamentals of Photonics* (John Wiley & Sons, Hoboken, 2019), 3rd ed.